# SIMULATION OF WELD SOLIDIFICATION CRACKING IN VARESTRAINT TESTS OF ALLOY 718

J. DRAXLER*, J. EDBERG*, J. ANDERSSON** and L-E. LINDGREN*

*Luleå University of Technology, 97187 Luleå, Sweden. Joar.Draxler@ltu.se, Jonas.Edberg@ltu.se, Lars-Erik.Lindgren@ltu.se
**University West, 46132 Trollhättan, Sweden. Joel.Andersson@hv.se

DOI 10.3217/978-3-85125-615-4-26

ABSTRACT

Several nickel-based superalloys are susceptible to weld solidification cracking. Numerical simulation can be a powerful tool for optimizing the welding process such that solidification cracking can be avoided. In order to simulate the cracking, a crack model inspired by the RDG model is proposed. The model is based on a crack criterion that estimates the likelihood for a preexisting pore in a grain boundary liquid film to form a crack. The criterion depends on the thickness and the liquid pressure in the grain boundary liquid film, as well as the surface tension of the pore. The thickness of the liquid film is computed from the macroscopic mechanical strain field of an FE model with a double ellipsoidal heat source. A temperature-dependent length scale is used to partition the macroscopic strain to the liquid film. The liquid pressure in the film is evaluated using a combination of Poiseuille parallel plate flow and Darcy's law for porous flows. The Poiseuille flow is used for the part of the grain boundary liquid film that extends into the region with liquid fraction less than 0.1, while Darcy's law is used for the rest of the liquid film that extends into the regions with liquid fraction greater than 0.1. The proposed model was calibrated and evaluated in Varestraint tests of Alloy 718. Crack location, width, and orientation were all accurately predicted by the model.

Keywords: Solidification cracking, Hot cracking, Varestraint testing, Computational Welding Mechanics, Alloy 718

## INTRODUCTION

Several nickel-based superalloys are susceptible to weld hot cracking [1]. These cracks can act as sites for the initiation of fatigue and corrosion cracking. Weld hot cracking involves cracks that form during the solidification of the weld. It consists of two different types of cracking: solidification cracking (SC) and liquation cracking [2]. In this study, we only consider SC. SC forms in the fusion zone of the weld via fracture of liquid films. The liquid films are normally grain boundary liquid films (GBLFs). The crack formation depends on a complicated interplay between metallurgical, thermal, and mechanical factors [3].

Numerical simulation can be a powerful tool to study the susceptibility of a welding process to SC. In order to model the cracking, a model for the crack initiation is needed. Several models have been developed, often for casting, wherein SC is also a problem and is referred to as hot tearing [4, 5]. However, most of these models suffer from one common shortcoming, in that they fail to address how the liquid is fractured [5]. One exception is the model by Rappaz, Drezet, and Greamaud (the RDG model) [6], which estimates the inter-dendritic liquid pressure drop to cavitation. Suyitno et al. [7] compared eight different hot cracking criteria in a simulation of DC casting of aluminum alloys and found that the RDG model best reproduced experimental trends. Nonetheless, this model is limited by some shortcomings. Rappaz has stated the two main approximations used [8]: first, the rheology of the mushy zone is not accurately accounted for; second, the localization of strains and feeding at grain boundaries is not considered. Coniglio et al. [9] pointed out a third shortcoming of the RDG model: cavitation as a liquid fracture mechanism is not likely to occur except at elevated levels of hydrogen content.

The second and third shortcomings have been addressed by Coniglio et al. [9]. Instead of assuming that strain is localized evenly between dendrites, as in the RDG model, they assumed it to be localized evenly between grains, and instead of assuming cavitation as the liquid fracture mechanism, they considered the cracking to originate from pore growth.

The assumption that cracking originates from pores agrees with recent in situ experiments. Puncreobutret et al. [10] performed in situ hot tensile tests of an Al-15 wt% Cu alloy. Using fast synchrotron X-ray microtomography, they observed that the cracking grew from pre-existing voids and internally nucleated voids. Aucott et al. [11] have studied Varestraint testing in situ with high-energy synchrotron X-ray microtomography of steel. In agreement with Puncreobutret, they also observed that the cracking was initiated from internal voids.

In this study, we present a model for weld SC that is inspired by the RDG model and the improvements made to this model by Coniglio. The model addresses all three aforementioned shortcomings of the RDG model to some degree. It was calibrated and evaluated in Varestraint tests of Alloy 718. Both crack location and crack width predicted by the model were in good agreement with experimental data.

## MODEL DEVELOPMENT

The development of the model used for estimating the risk of SC in a given GBLF is presented below. First, the crack criterion is introduced, and then the method for computing the GBLF pressure, which is required to calculate the crack criterion, is presented.

### PORE FRACTURE MODEL

As was discussed earlier recent in situ experiments have indicated that SC forms from voids that grow into cracks. In this study, we assume that SC initiates from small pores in GBLFs which then grow into cracks when the GBLF pressure drops and/or GBLF thickness increases due to tensile strain. We assume that for each point on the axis of a given GBLF, there is a pore that extends across the thickness of the GBLF and has the potential to grow into a crack. The nucleation of these pores is not considered; instead, the conditions for how such a pre-existing pore can grow into a SC is studied.

#### *Equilibrium pore shape*

To simplify the study of how a pore can grow into a crack, a GBLF with parallel solid-liquid interfaces was studied. In such a GBLF, a SC is assumed to form from a pre-existing gas capillary bridge which grows into a crack when the pressure and the thickness of the GBLF change (see Fig. 1). The capillary bridge is assumed to be rotationally symmetric about the $z$-axis and symmetric about the $z = 0$ plane.

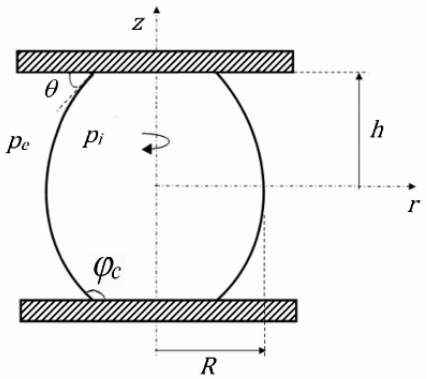


**Fig. 1** Coordinates used for describing the profile shape of the gas bridge.

Let $r$ and $z$ be the coordinates that trace out the profile of the pore, and let $R$ be the radius of the pore at its equator (see Fig. 1). The equilibrium shape of the capillary bridge can be obtained from the Young-Laplace equation, which for the rotational symmetric bridge gives [12]:

$$z(\phi) = \int_{\pi/2}^{\phi} \frac{1 - p\cos^2(v)}{\sqrt{(p(\sin(v)-1)+1)(p(\sin(v)+1)-1)}}\, dv \quad (1)$$

where $\phi$ is the dimensionless variable

$$sin(\phi) = \frac{r}{R} \tag{2}$$

and $p$ is the dimensionless capillary pressure

$$p = \frac{sin(\phi_c)\, sin(\theta) - 1}{sin^2(\phi_c) - 1} \tag{3}$$

$\theta$ is the contact angle between the pore interface and the solid-liquid interface (see Fig. 1). $\phi_c$ is the value of $\phi$ at the solid-liquid inteface, which can be determined by solving Eq. (1) for $\phi$ when $z$ is equal to half the GBLF thickness ($h$). This can be done using a numerical root finder such as MATLAB's fzero.

By applying the ideal gas law, and again using the Young-Laplace equation, the external pore pressure ($p_e$) can be obtained as a function of the dimensionless capillary pressure $p$ (Eq. (3)), the pore radius R, and the volume of the pore V :

$$p_e = \frac{p_{i0} V_0}{V} - \frac{2\gamma_{gl}}{R} p \tag{4}$$

where $\gamma_{gl}$ is the interfacial energy of the liquid-gas pore interface, and $p_{i0}$ and $V_0$ are the initial pressure and volume of the pre-existing pore. It is assumed that no gas diffuses to the pore during the solidification. By letting the pore radius $R$ in Eq. (4) go to infinity, the external pore pressure becomes:

$$p_{e,\infty} = \lim_{R \to \infty} p_e = -\frac{\gamma_{gl} cos(\theta)}{h} \tag{5}$$

How $p_e$ varies with $R$ for different values of $p_{i0}$ is shown in Fig. 2a. The values $h =$ 2.5 µm, $\gamma_{gl} = 1$ J/m$^2$, $\theta = 10°$, and $R_0 = 2h$ were used in the plot. Here, $R_0$ is the pore radius of the initial pre-existing pore. As can be seen in the figure, the external pressure required to keep the pore in equilibrium at its initial growth is highly dependent on $p_{i0}$. Fig. 2b shows how $p_e$ varies with $R$ for different values of $h$, using the same parameter values as in the Fig. 2a but with $p_{i,0} = 0$ bar. As can be seen in the figure, the pressure required for a large pore to be stable is highly dependent on the GBLF thickness. A large pore can be stable at a much lower pressure drop in a wide GBLF than in a narrow GBLF.

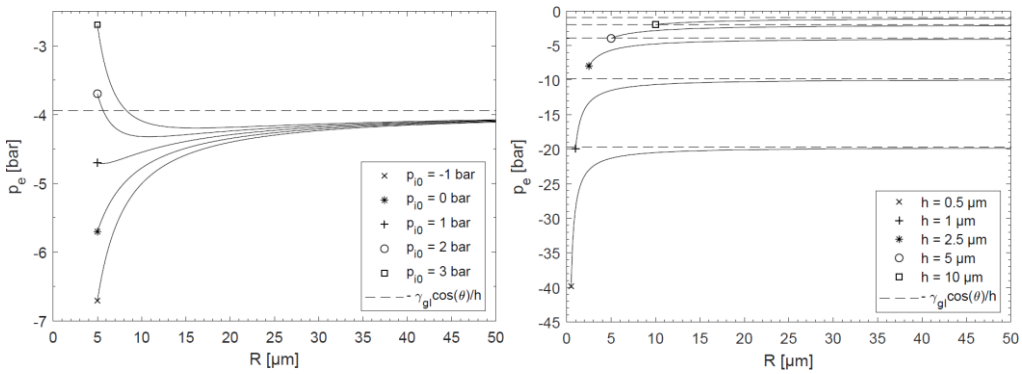


(a) (b)

**Fig. 2** $p_e$ as a function of $R$ for: (a) different values of $p_{i,0}$, (b) different values of $h$.

More details about derivations of the above equations and the influence of the different parameters on the relation between $p_e$ and $R$ can be found in [12].

### *Crack criterion*

From the relation between the radius and external pressure of a stable pore in a GBLF with parallel interfaces (Eq. (4)), it can be shown that the external pressure of a stable pore never exceeds $p_{e,\infty}$ (Eq. (5)), unless the initial pore pressure and size are large. This can be used to construct a conservative pressure-based crack criterion for SC. We assume that a large stable pore in a GBLF can form as soon as the liquid pressure in the GBLF drops below $p_{e,\infty}$. A crack initiation index (CII) can then be defined as the ratio between the liquid pressure drop and the liquid pressure drop to $p_{e,\infty}$:

$$CII = \frac{p_{atm} - p}{p_{atm} - p_{e,\infty}} \tag{6}$$

where $p_{atm}$ is the atmospheric pressure, and $p$ is the liquid pressure in the GBLF, which is computed in the absence of the pore via the pressure model described below. A CII value larger than 1 indicates that crack initiation is predicted.

A CII value larger than 1 does not guarantee the formation of a permanent crack. For example, if the liquid pressure drop decreases, the surface tension of the pore can contract and close the pore. In this study, we consider the formation of a permanent crack to occur when the CII value is larger than 1 at the location of the solidus isotherm. If we assume that all the remaining liquid instantly solidifies at the solidus temperature, a crack that is passed by this isotherm can never be healed, and therefore becomes a permanent crack in the solid phase. Thus, SC is considered to occur in a GBLF if the CII value is larger than 1 at the terminal solidification location of the GBLF. The crack initiation length (CIL) can then be defined as the length along a GBLF where the CII value is larger than 1, as follows:

$$CIL = \int_{s_{ci}} ds \tag{7}$$

where $s$ is a coordinate along the GBLF axis, which, for example, can be along the columnar grain growth direction in a TIG weld. The integration path $s_{ci}$ is the part of the GBLF axis where the CII value is larger than 1 at the intersection with the solidus isotherm, as shown in Fig. 3.

We consider the CIL of a GBLF to be the part of the GBLF where a pore, if its initial size is large enough, can form a permanent crack in the solid phase. Thus, if a large enough pre-existing pore is located within this region of the GBLF, it is assumed to cause crack initiation.

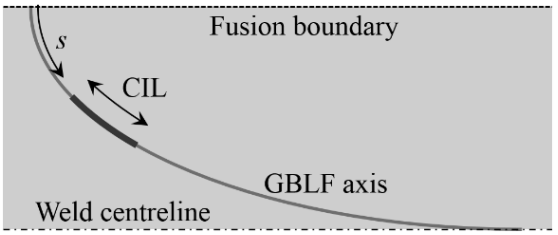


**Fig. 3** Schematic representation of the CIL of a GBLF. The welding direction is from left to right. The GBLF axis shown is located between columnar grains that extend from the fusion boundary and aligns with the weld centerline. The GBLF axis shown is located close the weld surface.

## GBLF PRESSURE MODEL

In order to compute the susceptibility to cracking for a given GBLF using the criterion in Eq. (7), the liquid pressure and the thickness of the GBLF must be known. These quantities were estimated as follows.

### *GBLF orientation*

To compute the liquid pressure in a given GBLF, the orientation and shape of the GBLF must be known. In this study, we only consider a fully columnar dendritic microstructure in the fusion zone, which can result from low welding speed with TIG welding [13]. In order to estimate the orientation of a GBLF in this microstructure, it was assumed that the columnar grains were always growing normal to the liquidus isotherm, with zero undercooling to solidification. This results in long curved grains that extend from the fusion boundary to the weld centerline. The axis of such a grain can be determined from [13]:

$$\frac{d\boldsymbol{r}}{dt} = -\frac{1}{G_L^2}\frac{\partial T_L}{\partial t}\boldsymbol{G}_L \tag{8}$$

where $\boldsymbol{r(t)}$ is the location of the grain tip, $\boldsymbol{G}_L$ is the temperature gradient at the tip, and $T_L$ is the liquidus temperature. The longitudinal axis of a GBLF was defined to be the same as the axis of an adjacent grain. By giving a point r0 on the axis, the GBLF axis was computed by integrating Eq. (8) with a fourth-order Runge-Kutta method (see Fig. 4). The temperature field required in the integration was obtained from post-processing of the FE

model of the weld process described below. As will be explained later, the transverse direction to a GBLF was defined as the direction of maximum strain rate, normal to its longitudinal axis.

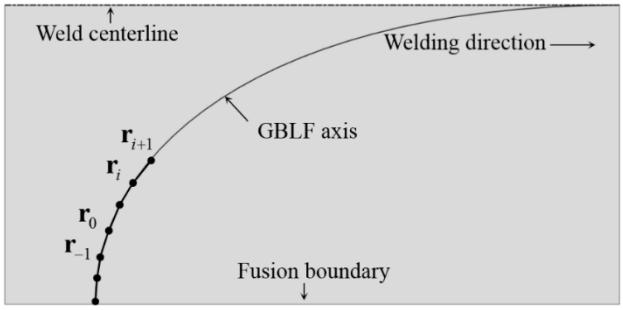


**Fig. 4** Schematic showing the procedure of integrating the longitudinal axis of a GBLF that passes the point $r_0$.

*GBLF solidification*

The solidification of the liquid in the given GBLF was approximated with a multicomponent Scheil-Gulliver model. The undeformed GBLF is assumed to be bounded by columnar dendrites separated by the primary dendrite arm spacing $\lambda_1$ (see Fig 5a). In order to simplify the modeling of the solidification process, the interfaces of the GBLF were assumed to be planar, separated by the undeformed GBLF thickness $2h_0$ (see Fig. 5b) [14].

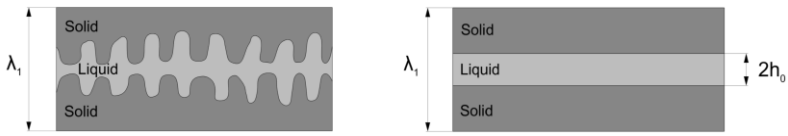


**Fig. 5** (a) Schematic representation of a GBLF with dendritic interfaces, (b) simplified GBLF with planar interfaces.

The undeformed half GBLF thickness ($h_0$) can then be written as:

$$h_0 = \frac{\lambda_1}{2}(1 - f_s) \tag{9}$$

where $f_s$ is the volume fraction of solid. $f_s$ was determined for Alloy 718 with the thermodynamic software Thermo-Calc [14]. The resulting volume fraction of solid vs. temperature curve is shown in Fig 6.

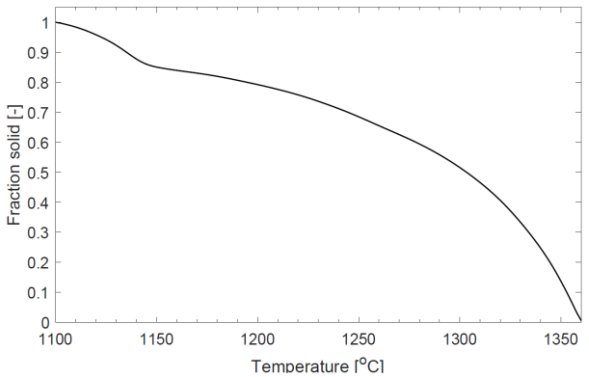


**Fig. 6** Volume fraction of solid of Alloy 718 as a function of temperature.

The primary dendrite arm spacing $\lambda_1$ in Eq. (9) was computed from the following simple one-parameter expression [8,13]:

$$\lambda_1 = \frac{C_1}{(G_L)^{1/2}(R_L)^{1/4}} \tag{10}$$

where $R_L$ is the solidification velocity at the grain tip and $C_1$ is a calibration parameter.

The solidification speed v* of the solid-liquid interface for the idealized GBLF shown in Fig. 5b can now be computed by the negative time-derivative of h0 (Eq. (9)), which gives:

$$v^* = \frac{\lambda_1}{2}\frac{df_s}{dT}\frac{dT}{dt} \tag{11}$$

where $T$ is obtained from the FE model of the weld process. The liquid that remains when the temperature drops below the solidus temperature was assumed to solidify instantly.

*GBLF thickness*

During the solidification of the weld, thermal tensile strains can strongly localize in the weak GBLFs. The deformed GBLF thickness, 2h, at an arbitrary location on the axis of the GBLF, was computed as follows. At the given location on the GBLF axis, all macroscopic mechanical strain normal to the axis that occurs during the infinitesimal time interval dt and within a region with diameter $2h + l_0$ surrounding the GBLF axis, is assumed to localize in the GBLF (see Fig. 7). The length scale l0 represents the amount of surrounding solid phase of the GBLF that can carry tensile loads. The solid phase is assumed to be much stiffer than the liquid phase, such that all macroscopic mechanical strains localize in the GBLF. Let εm be the macroscopic mechanical strain tensor obtained from the FE model of the weld process. Then the velocity of the solid-liquid interface of the GBLF can be written as (see Fig. 7):

$$\frac{dh}{dt} = \left(h + \frac{l_0}{2}\right)\frac{d\varepsilon^m_{\perp,max}}{dt} - v^* \tag{12}$$

where $v^*$ is the solidification velocity given by Eq. (11). $\dot{\varepsilon}^{m}_{\perp,max}$ is the largest macroscopic mechanical strain rate in a plane normal to the axis of the GBLF, and is evaluated on the GBLF axis. Thus, the normal direction of the GBLF is assumed to be parallel to the direction of $\dot{\varepsilon}^{m}_{\perp,max}$.

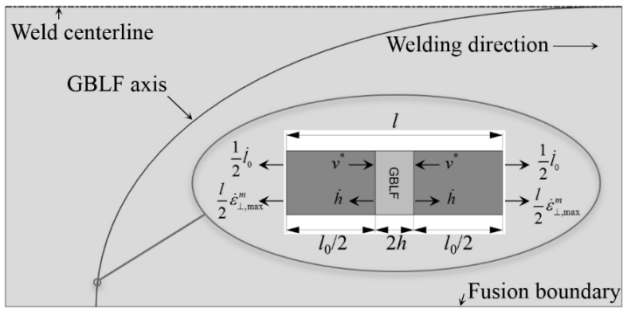


**Fig. 7** Strain localization in a GBLF.

The strain partitioning length $l_0$ depends on the coalescence and the interlocking of dendrites and grains. In this study, $l_0$ was estimated from the temperature and the primary dendrite arm distances as follows. At the liquidus temperature $T_l$, there is no strain localization, and thus $l_0 = 0$ at $T_l$. At the coherent temperature $T_c$, the dendrites of individual grains have started to coalesce, and therefore the dendritic structure can carry small tensile loads. In this case, $l_0$ was assumed to have length equal to the width of the primary dendrite arm spacing. Below $T_c$, strains were assumed to localize between grain clusters. At the solidus temperature $T_s$, $l_0$ was assumed to have the same size as the grain clusters. The grain cluster size is not known, and was assumed to be proportional to the primary dendrite arm distance:

$$l_0(T_s) = C_2\lambda_1 \tag{13}$$

where $C_2$ is a parameter that is determined by inverse modeling [13,14]. At temperatures between $T_s$, $T_c$, and $T_l$, $l_0$ was assumed to vary linearly. Fig. 8 show the values of $l_0$ used in this study.

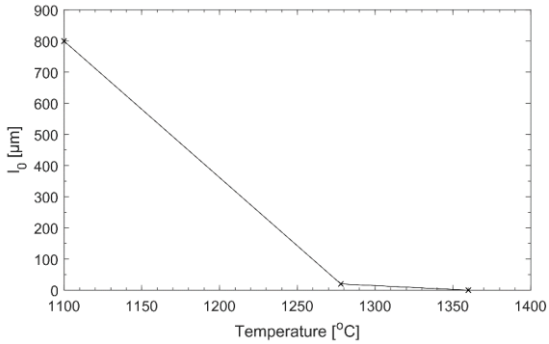


**Fig. 8** $l_0$ as a function of temperature for Alloy 718.

## GBLF PRESSURE

By knowing the orientation, solidification velocity, and thickness of the GBLF from the above expressions, the liquid pressure in the GBLF can be computed as follows. The liquid flow in a GBLF is assumed to be in the direction of the GBLF axis. Moreover, the flow in a given GBLF is assumed to be confined solely to that GBLF, and thus no flow interactions with other GBLFs are considered. Taking the mass balance of an infinitesimally thin cross-section volume element of a given GBLF gives [13]:

$$\frac{d}{ds}(h\bar{v}) = -(1+\beta)v^* - \frac{dh}{dt} \tag{14}$$

where $\bar{v}$ is the average flow velocity, $\beta$ is the solidification shrinkage factor, and $s$ is a curved coordinate along the GBLF axis as shown in Fig. 3. For the part of the GBLF that extends into regions with liquid fraction below 0.1, a Poiseuille parallel plate flow is used, which gives:

$$\bar{v} = -\frac{h^2}{3\mu}\frac{dp}{ds}, \quad f_l \leq 0.1 \tag{15}$$

where $\mu$ is the dynamic viscosity and $p$ is the liquid pressure. For the rest of the GBLF, which extends into regions with liquid fraction greater than 0.1, the flow is assumed to be governed by Darcy's law for porous flows:

$$\bar{v} = -\frac{K_{\parallel}}{\mu f_l}\frac{dp}{ds}, \quad f_l > 0.1 \tag{16}$$

where $K_{\parallel}$ is the longitudinal permeability of the columnar dendrite structure. The permeability relation developed by Heinrich and Poirier [15] for columnar dendritic structures is used:

$$K_{\|} = \begin{cases} 3.75 \times 10^{-4} f_1^2 d_1^2, & f_l \leq 0.65 \\ 2.05 \times 10^{-7} \left[\frac{f_l}{1-f_l}\right]^{10.739} d_1^2, & 0.65 < f_l \leq 0.75 \\ 0.074 \left[log\left(\frac{1}{1-f_l}\right) - 1.49 \right. & \\ \left. +2(1-f_l) - 0.5(1-f_l)^2\right] d_1^2, & 0.75 < f_l \leq 1.0 \end{cases} \quad (17)$$

where $d_1$ is the spacing between the dendrites. In order to account for the increase in permeability at the GBLF that occurs when deformation is localized to the GBLF, d1 and f_l in Eq. (17) are replaced by [13]:

$$d_1^* = \lambda_1 + 2h - 2h_0 \quad (18)$$

and

$$f_l^* = 1 - \frac{\lambda_1^2 (1-f_l)}{d_1^{*2}} \quad (19)$$

The pressure in the GBLF was obtained by integrating Eq. (14) twice along the axis of the GBLF, with $\bar{v}$ given by Eqs. (15) and (16). The integrand was computed from the temperature and mechanical strain fields obtained from post-processing of the FE model of the weld process, evaluated at Lagrangian sample points on the GBLF axis. For a given time, the integration was performed between the intersections of the solidus and liquidus isotherms with the GBLF axis [13]. At the junction between the Poiseuille and Darcy flow regions, continuous pressure and flow were assured. In the integration of Eq. (14), the following two boundary conditions were used. At the liquidus isotherm, the liquid pressure was assumed to be the equal to the atmospheric pressure. At the solidus isotherm, the pressure gradient was given by [13]:

$$\frac{dp}{ds} = \left(\frac{3\mu\beta}{h^2}\frac{ds}{dt}\right)\Big|_{s=s_{T_s}} \quad (20)$$

where $ds/dt$ is the projected solidification velocity at the solidus temperature, in the direction of the GBLF axis. Eq. (20) corresponds to the pressure drop at the end of the GBLF due to the liquid flow caused by solidification-induced shrinkage of the remaining liquid at the end of the film.

The dynamic viscosity of Alloy 718 in the solidification interval was obtained from the software package JMatPro [14].

## GAS-LIQUID INTERFACE ENERGY

To compute the CII value in Eq. (6), the factor $\gamma_{gl} \cos\theta$ must be known. It is assumed that the solid phase is sufficiently wetted by the liquid phase, such that the contact angle is small. In this case, $\cos\theta$ is approximately 1.

The surface tension of Alloy 718 has been measured by the oscillating drop method [14]. It varies linearly with temperature, in the temperature interval 1350 < $T$ < 1600 °C, according to the function:

$$\gamma\ mNm^{-1} = 1800 - 0.11(T - 1725℃) \quad (21)$$

This equation was used to estimate $\gamma_{gl}$. The equation was assumed to be valid for extrapolation down to the solidus temperature.

## MATERIAL AND EXPERIMENTAL PROCEDURES

The SC model in this study was calibrated and evaluated with Varestraint tests of Alloy 718. The tests are described below, along with some relevant properties of Alloy 718.

### ALLOY 718

Alloy 718 is a high-strength, corrosion-resistant nickel-chromium alloy used between -250 and 700 °C. It was developed in the early 1960s and is used in a wide range of applications such as components for liquid fuel rockets, rings, casings, and various formed sheet metal parts for aircraft and land-based gas turbine engines, and in cryogenic tanks. It is the predominant nickel-iron-based superalloy, representing nearly half of the total quantity of superalloys used worldwide. Typical composition limits of Alloy 718 are shown in Table 1.

**Table 1** Chemical composition limits of Alloy 718 (wt%).

| Ni | Fe | Cr | Nb | Mo | Ti | Al | Co | C | Mn | Si | P | S | B | Cu |
|---|---|---|---|---|---|---|---|---|---|---|---|---|---|---|
| 50.00 | Bal. | 17.00 | 4.75 | 2.80 | 0.65 | 0.20 | - | - | - | - | - | - | - | - |
| 55.00 | Bal. | 21.00 | 5.50 | 3.30 | 1.15 | 0.80 | - | 0.08 | 0.35 | 0.35 | 0.015 | 0.015 | 0.006 | 0.30 |

The matrix consisting of approximately 50% nickel, 20% chromium, and 20% iron is strengthened primarily by the 5% niobium content. Niobium forms the main strengthening precipitate $\gamma''$ ($Ni_3Nb$). In an age-hardened condition, Alloy 718 contains approximately 20% $\gamma''$ phase.

Alloy 718 is reported to be resistant to strain-age cracking, owing to the sluggish precipitation kinetics of its principal strengthening precipitate γ". However, it is not free of weldability challenges, including SC.

## THE VARESTRAINT TEST

The Varestraint test was developed in the 1960s by Savage and Lundin at Rensselaer Polytechnic Institute. This test allows the study of the susceptibility of a specimen to hot cracking via a systematic procedure requiring only small and simple test specimens. The influences of the material, the welding process, and the constraint factors on the hot cracking behavior can be identified. The basic procedure is to rapidly apply an augmented strain during the welding of a plate. The amount of augmented strain $\varepsilon_{aug}$ depends on the material thickness and the radius of the die block, according to the following equation:

$$\varepsilon_{aug} = \frac{t}{2R+t} \tag{22}$$

where $t$ is the sample thickness and $R$ is the radius of the die block. The bending is applied along the length of the weld made on the sample. The augmented strain can be varied simply by changing the die block radius.

## EXPERIMENTAL PROCEDURE

The derived model for SC was calibrated and evaluated using Varestraint tests. The test setup is shown in Fig. 9a. Figs. 9b and c show the test plate in the press before and after bending, respectively.

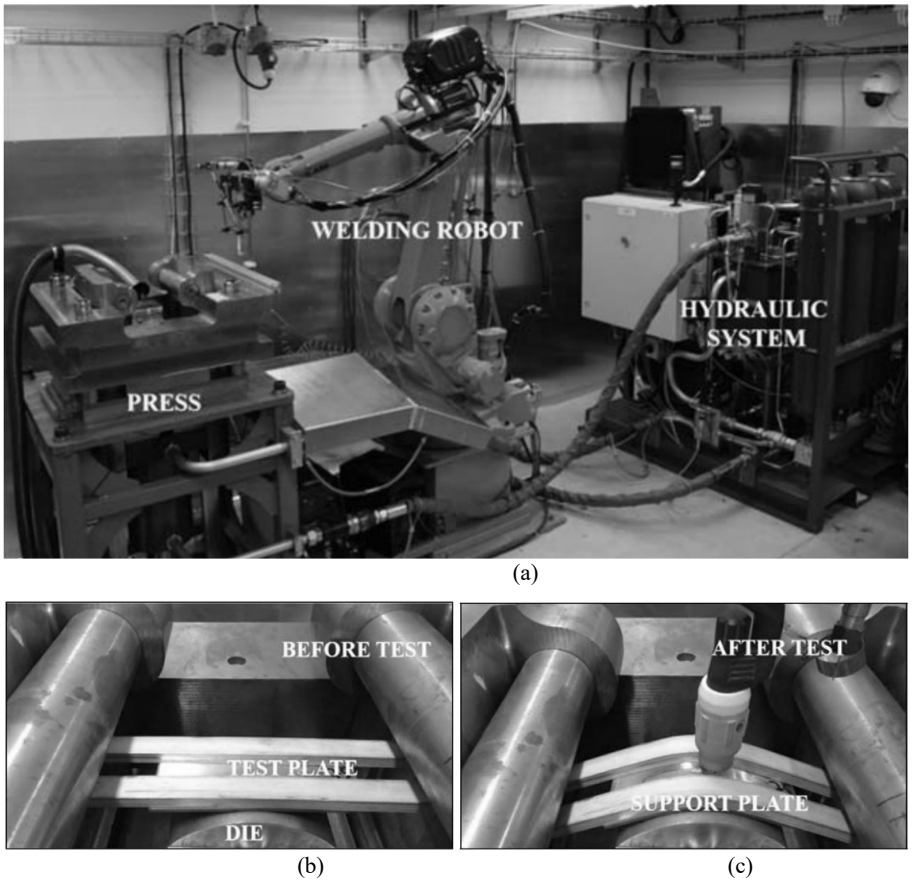


**Fig. 9** Varestraint test equipment used in the experiments.

In the test, the plate is bent over the die block by vertical displacement of the rollers while the die block remains stationary. Support plates are used to reduce kinking of the test plate. All tests were performed on 3.2 mm-thick plates with dimensions of 60×150 mm. The dimensions of the support plates were 10×20×300 mm. The starting position of the weld was 40 mm from the contact point between the plate and the die block. The bending was initiated when the weld electrode passed over the apex of the die block (i.e., the contact point between the plate and die). Welding was continued for 5 s after bending was initiated. Autogenous TIG welding was used for the tests. The welding current was 70 A, with automatic voltage regulation. Based on an estimated voltage of 10 V, the weld power was 700 W. The welding speed was 1 mm/s and the stroke rate was 10 mm/s. The Varestraint test parameters are summarized in Table 2.

**Table 2** Varestraint parameters.

| | |
|---|---|
| Welding speed | 1 mm/s |
| Welding current | 70 A |
| Arc length | 2 mm |
| Gas flow (Ar) | 15 L/min |
| Weld length | 40 mm |
| Weld offset | 5 mm |
| Stroke rate | 10 mm/s |

Four different die block radii were used, resulting in 0.3%, 0.4%, 0.8%, and 1.1% augmented strains. The test plates underwent two different heat treatments prior to the welding: the first was solution annealing at 954 °C for 1 h, and the second consisted of solution annealing at 1050 °C for 3 h followed by furnace cooling to 954 °C, where it was held for 1 h. Table 3 shows the details of the Varestraint samples used in this study.

**Table 3** Sample parameters.

| Sample # | Augmented strain (%) | Heat treatment |
|---|---|---|
| 3 | 1.1 | 954 °C (1 h) |
| 6 | 1.1 | 1054 °C (3 h) + 954 °C (1 h) |
| 20 | 0.8 | 954 °C (1 h) |
| 21 | 0.8 | 954 °C (1 h) |
| 23 | 0.8 | 1054 °C (3 h) + 954 °C (1 h) |
| 24 | 0.8 | 1054 °C (3 h) + 954 °C (1 h) |
| 37 | 0.4 | 954 °C (1 h) |
| 38 | 0.4 | 954 °C (1 h) |
| 40 | 0.4 | 1054 °C (3 h) + 954 °C (1 h) |
| 41 | 0.4 | 1054 °C (3 h) + 954 °C (1 h) |
| 42 | 0.4 | 1054 °C (3 h) + 954 °C (1 h) |
| 58 | 0.3 | 1054 °C (3 h) + 954 °C (1 h) |

The location, length, and width of the surface cracks in the fusion zone were measured using a stereo microscope. No cracks were found in any of the samples with 0.3% and 0.4% augmented strains. Even though no cracks were found in the 0.4%-strain test samples, a strain of 0.4% was considered to be the threshold strain for crack initiation [14].

## FINITE ELEMENT MODEL

The temperature field and macroscopic mechanical strain fields are required in order to evaluate the SC model derived in this study. Both were obtained from coupled thermo-mechanical finite element models of Varestraint tests using the software MSC Marc. The FE models use a double ellipsoid heat source as the weld heat input. Thermophysical properties of the mushy zone in the FE models were obtained from mixture rules of the solid and liquid phases. Four different material models, each active in a different temperature range, were used to describe the inelastic behavior in the fusion zone and the partially melted zone in the FE models. Due to the symmetry at the weld centerline, only one half of the Varestraint test was modeled. In the region of the Varestraint test where SC occurs, an element size of approximately 100 μm was used in order to resolve the

temperature and strain fields. Fig. 10a shows the meshed model and Fig. 10b shows the fine mesh used in the crack-susceptible region. The FE model is described in more detail in [14].

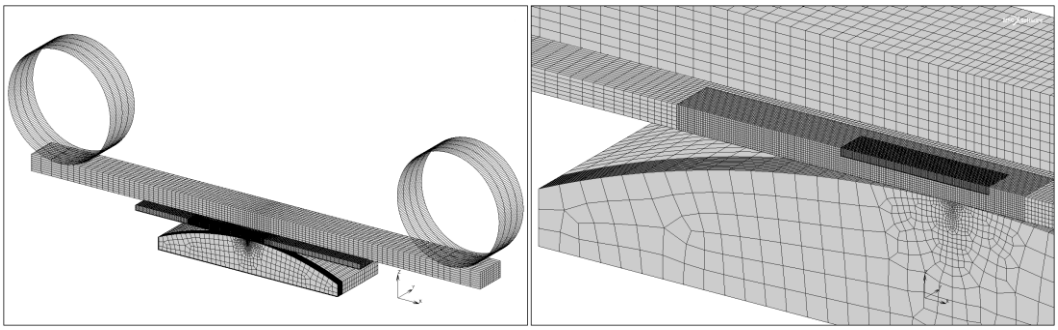

(a) (b)

**Fig. 10** (a) Meshed half-symmetric part of the Varestraint test and (b) mesh used in the region where cracking occurred.

## RESULTS

The proposed SC model was calibrated in a Varestraint test with 0.4% augmented strain, and then validated on tests with 0.8% and 1.1% strains. All properties were evaluated on GBLF axes on the surfaces of the weld, separated from each other at the fusion boundary by approximately 1 mm. The evaluation was performed on the weld surface, as the susceptibility to cracking is considered to be highest at this area because the tensile strains from the bending are largest on the weld surface. It is also easier to evaluate experimental results on the weld surface, as no cutting is required. The x and y coordinates in the plots represent the distances from the weld start and the weld centerline, respectively. The welding direction was from left to right. When computing the GBLF pressure, the presence of the pore in the GBLF was not considered. The effect of surface interaction on the flow in GBLFs was not considered either; in other words, the evaluation was considered to have taken place close to the weld surface but not so close that it would be disturbed by the surface.

### GBLF AXES

Fig. 11 shows the computed GBLF axes from Eq. (8), at the weld surface in a Varestraint test with 0.4% augmented strain. They are separated by 1 mm at the fusion boundary, and together cover the entire region where surface cracks occurred. For the leftmost axis, the locations of the sample points which were used to evaluate the temperature and mechanical strains using the FE model, are shown with crosses.

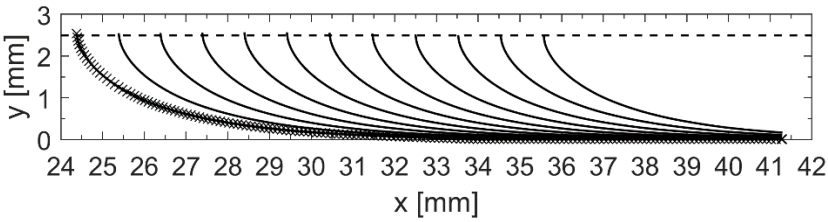


**Fig. 11** Computed GBLF axes at the weld surface in the Varestraint test with 0.4% augmented strain. The axes are separated by 1 mm at the fusion boundary. Only one half of the symmetric weld is shown.

## CALIBRATION

In order to estimate the susceptibility of the sample to cracking, the parameters $C_1$ and $C_2$ must be calibrated. $C_1$, which is related to $\lambda_1$ via Eq. (10), was calibrated such that the computed value agreed with the measured value at a location approximately 30 mm from the weld start, 1 mm from the fusion boundary, and 0.1 mm below the weld surface. $C_2$ was calibrated such that a maximum CIL of 300 μm was obtained for the 0.4%-strain test. As was previously mentioned, an augmented strain of 0.4% was considered to be the threshold value for crack initiation. More details of the calibration can be found in [14].

## CIL

Fig. 12a shows the computed CIL for the 0.8%-strain tests, together with the crack locations in four experimental test specimens with the same strain. The computed CIL for the GBLF tracks shown covers all cracks found in the experiments. Most of the cracks were located 0.5 - 2 mm from the weld centerline. Interestingly, it is also this region that has the GBLFs with the highest CILs. It is also interesting to note that the crack orientations did not diverge too much from the GBLF axes, which indicates that the assumption that grain growth occurred in the direction normal to the liquidus isotherm was a fairly good approximation in this situation.

Fig. 12b shows the computed CILs for the 1.1%-strain test together with the crack locations in two test specimens with the same strain. The computed CIL for the GBLF tracks shown almost covers all cracks found in the experiments. Similarly to the result for the 0.8%-strain test, the majority of the cracks were located 0.5 - 2 mm from the weld centerline. Again, it is in this region that the model predicts the highest CILs. The agreement between the crack orientations and the GBLF axes in this test is fairly strong.

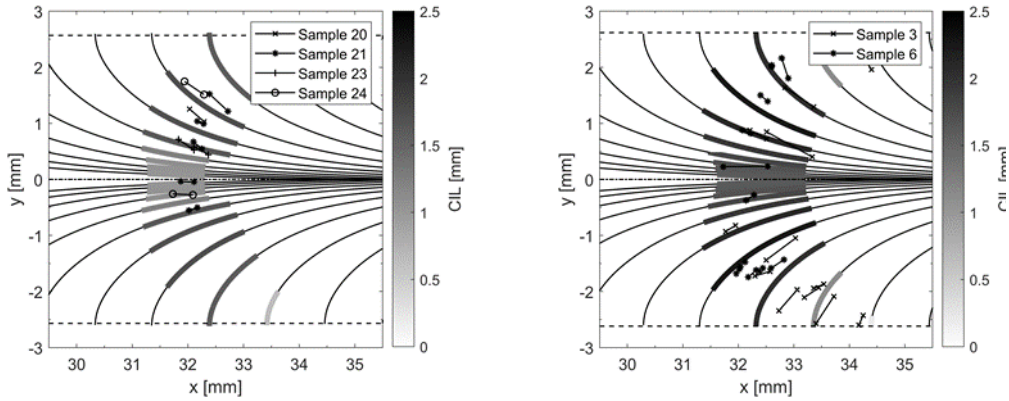


(a) (b)

**Fig. 12** CIL of (a) 0.8% and (b) 1.1% augmented strain tests.

## CRACK WIDTH

In order to evaluate the strain localization model used in this work, the crack widths predicted by the model were compared to those measured experimentally. The predicted crack width was computed as the GBLF thickness at the moment when the temperature dropped below the solidus temperature. Fig. 13a shows the computed and measured crack widths for the 0.8%-strain tests. The agreement between the computed and measured crack widths is pretty strong.

The agreement between the computed and measured crack widths is also fairly good for the 1.1%-strain test, which is shown in Fig. 13b. However, there is one crack, approximately 20 μm wide, that is considerably larger than the rest of the cracks. The reason for this may be that deformation continued to localize in the crack at temperatures below the solidus temperature, a phenomenon which is not accounted for in the model. The strong agreement between the computed and measured crack widths is an indication that the strain localization model used in this experiment worked fairly well under these conditions.

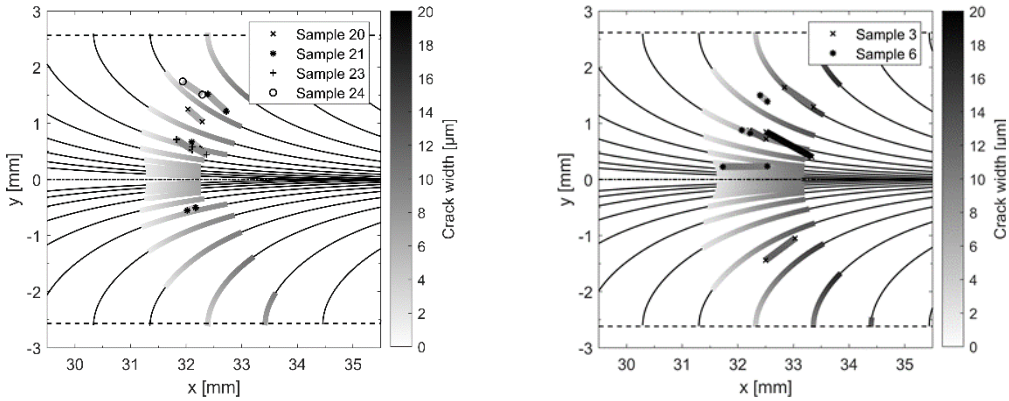


(a) (b)

**Fig. 13** Crack width in samples subjected to (a) 0.8% and (b) 1.1% augmented strain tests.

## CONCLUSIONS

Simulations of weld solidification cracking in Varestraint tests of Alloy 718 were performed, and good accuracy was achieved. The physical based crack criterion is capable of pinpointing the region where SC will occur. The strain localization model used in this work predicts crack widths that are in good agreement with experimental measurements. The computed orientations of the grain boundaries agree fairly well with the orientation of the intergranular cracks observed experimentally.

## ACKNOWLEDGEMENTS

The authors gratefully acknowledge financial support from the NFFP program operated by the Swedish Armed Forces, the Swedish Defense Material Administration, and the Swedish Governmental Agency for Innovation Systems (project numbers: 2013-01140 and 2017-04837). Senior lecturer Paul Åkerström at Luleå Technical University is also gratefully acknowledged for his invaluable support and guidance. Moreover, the authors sincerely thank Rosa Maria Pineda Huitron and Laetitia Lefevre from the Material Science Department at Luleå Technical University for their assistance in evaluating the experimental Varestraint tests.

## REFERENCES

[1] LIPPOLD, JOHN C., SAMUEL D. KISER, AND JOHN N. DUPONT: *Welding metallurgy and weldability of nickel-base alloys*. John Wiley & Sons, 2011.
[2] LIPPOLD, JOHN C: *Welding metallurgy and weldability: John Wiley & Sons, 2014.*
[3] KOU, SINDO: *Welding metallurgy.* John Wiley & Sons, 2003.
[4] ESKIN, D. G., AND L. KATGERMAN: *Mechanical properties in the semi-solid state and hot tearing of aluminum alloys.* Progress in Materials Science 49.5 (2004): 629-711.

[5] CONIGLIO, N., AND C. E. CROSS: *Initiation and growth mechanisms for weld solidification cracking.* International Materials Reviews 58.7 (2013): 375-397.
[6] RAPPAZ, M., J-M. DREZET, AND MET GREMAUD*: A new hot-tearing criterion.* Metallurgical and materials transactions A 30.2 (1999): 449-455.
[7] SUYITNO, W. H., AND L. KATGERMAN: *Hot tearing criteria evaluation for direct-chill casting of an Al-4.5 pct Cu alloy.* Metal Mater Trans A 36.6 (2005): 1537-1546.
[8] DANTZIG, JONATHAN A., AND MICHEL RAPPAZ: *Solidification.* EPFL press, 2009.
[9] CONIGLIO, N., AND CARL EDWARD CROSS: *Mechanisms for solidification crack initiation and growth in aluminum welding.* Metallurgical and Materials Transactions A 40.11 (2009): 2718-2728.
[10] PUNCREOBUTR, CHEDTHA, ET AL.: *Synchrotron tomographic characterization of damage evolution during aluminum alloy solidification.* Metallurgical and Materials Transactions A 44.12 (2013): 5389-5395.
[11] AUCOTT, L., ET AL.: *Initiation and growth kinetics of solidification cracking during welding of steel.* Scientific reports 7 (2017): 40255.
[12] JOAR DRAXLER, JONAS EDBERG, LARS-ERIK LINDGREN, JOEL ANDERSSON: *Simulation of Weld Solidification Cracking Part I: A Pore Based Crack Criterion,* Submitted for publication.
[13] JOAR DRAXLER, JONAS EDBERG, LARS-ERIK LINDGREN, JOEL ANDERSSON: *Simulation of Weld Solidification Cracking Part II: A Model for Estimation of Grain Boundary Liquid Pressure,* Submitted for publication.
[14] JOAR DRAXLER, JONAS EDBERG, LARS-ERIK LINDGREN, JOEL ANDERSSON: *Simulation of Weld Solidification Cracking Part III: Application to Varestraint tests of Alloy 718,* Submitted for publication.
[15] HEINRICH, JUAN C., AND DAVID R. POIRIER: *Convection modeling in directional solidification.* Comptes Rendus Mecanique 332.5-6 (2004): 429-445.